NIST Technical Note 1514

Metal Detector Studies: Research Materials

James Baker-Jarvis
Raian Kaiser
Michael D. Janezic
N. G. Paulter
K. L. Stricklett

Radio-Frequency Technology Division
Physics Laboratory
National Institute of Standards and Technology
325 Broadway
Boulder, Colorado 80305

August 2002

U.S. Department of Commerce
Donald L. Evans, Secretary

Technology Administration
Phillip J. Bond, Under Secretary of Commerce for Technology

National Institute of Standards and Technology
Arden L. Bement, Jr., Director

Certain commercial entities, equipment, or materials may be identified in this document in order to describe an experimental procedure or concept adequately. Such identification is not intended to imply recommendation or endorsement by the National Institute of Standards and Technology, nor is it intended to imply that the entities, materials, or equipment are necessarily the best available for the purpose.

National Institute of Standards and Technology Technical Note 1514
Natl. Inst. Stand. Technol. Tech. Note 1514, 36 pages (August 2002)
CODEN: NTNOEF

U.S. GOVERNMENT PRINTING OFFICE
WASHINGTON: 2002

For sale by the Superintendent of Documents, U.S. Government Printing Office
Internet: bookstore.gpo.gov Phone: (202) 512-1800 Fax: (202) 512-2250
Mail: Stop SSOP, Washington, DC 20402-0001

Contents

Metal Detector Studies: Research Materials

James Baker-Jarvis*, Raian Kaiser*
Michael D. Janezic*, N. G. Paulter†, K. L. Stricklett†

The purpose of the work described in this report was to develop and characterize phantom materials that mimic the electromagnetic properties of the human body. The materials were characterized from 100 Hz to 10 MHz and over a temperature range of 15 °C to 40 °C. Such phantoms will aid in the evaluation and assessment of the interaction of medical devices and metal objects or weapons with metal detectors. The materials studied were: (1) a mixture of potassium chloride in water, (2) a mixture of propylene carbonate, ethylene carbonate, and salts, (3) a semi-solid nano-composite material consisting of semi-solid silicone filled with carbon black particles, (4) a mixture of glycine, carrageenan, and potassium chloride, in water. The conductivities of all the materials were analyzed for stability over time and temperature dependence by use of both a conductivity meter and an open-ended coaxial line. We found that the conductivity of the carbon-black-silicone composite exhibited a percolation threshold as a function of carbon-black concentration. We also found that to obtain reproducibility, the carbon black mixture must be temperature annealed and consistently mixed. The silicone composite has the advantage of being more rugged than the liquid mixtures.

Key words: Conductivity; dielectric; frequency; nano-composite; permittivity; phantom.

*National Institute of Standards and Technology, Radio-Frequency Technology Division, MS 813.01, Boulder, CO e-mail:jjarvis@boulder.nist.gov
†National Institute of Standards and Technology, Electricity Division, MS 811, Gaithersburg MD

1. Introduction

The purpose of this report is to disseminate information on the development and characterization of materials that simulate the relevant electromagnetic (EM) properties of the human body. These materials when used as phantoms will allow evaluation and assessment of the interaction of personal medical electronic devices (PMEDs) and metal weapons with magnetic fields generated by hand-held (HH) and walk-through (WT) metal detectors. The goal was to study various mixtures of materials that simulate the relevant EM properties of human body tissue over the frequency range of 100 Hz to 10 MHz and a temperature range of 15 °C to 40 °C.

2. Overview of the Problem

The dielectric properties of human tissues have been studied extensively over the years. The range of conductivities that occur in the human body are well known. Therefore phantom materials that simulate the human body's electrical properties play a crucial role. In the past, phantoms have been used for: (a) studies on the low-frequency electromagnetic interaction with the human body, (b) health effects of microwaves, and (c) interaction of wireless transmitters with human tissue [1].

The effects of electromagnetic waves on biological tissues are related to the conductivity and dielectric properties of tissues. Interactions of magnetic fields with materials are related to the permeability, $\mu^* = \mu_0(\mu_r' - j\mu_r'')$, where $\mu_0 = 4\pi \times 10^{-7}$ (H/m), and conductivity σ (S/m) of the object in a metal detector. Time varying magnetic fields of a metal detector interact with metallic objects by inducing eddy currents ($\mathbf{J} = \nabla \times \mathbf{H}$) in objects that modify the incident magnetic field (see figures 1 and 2). Although the permittivity $\epsilon^* = \epsilon_0(\epsilon_r' - j\epsilon_r'')$, where $\epsilon_0 = 8.85 \times 10^{-12}$ (F/m), does not directly enter the equations for the surface resistance, the permittivity of the material determines the impedance and thereby affects the reflectivity of an incident wave from the interface of the object and air.

A magnetic field incident on the human body also generates eddy currents in the tissues, depending on their conductivity, but of much smaller magnitude than in metals. Due to the conductivities of the materials in the body, the incident magnetic fields attenuate as they pass into tissues. In order to model the response of a metal detector to a PMED or weapon, we need to understand the conductivity of the medium in which the device is immersed and also the permeability and conductivity of the PMED or weapon. Potential electromagnetic interference with implant devices relates to how deeply the fields penetrate the human body and the mismatch of impedance between the air and body. At low frequencies the fields

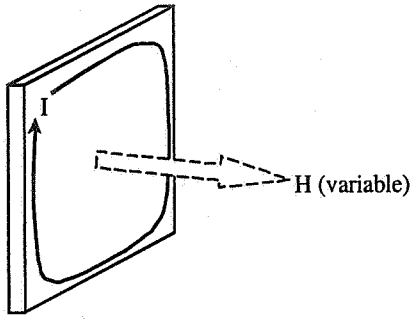

Figure 1. Eddy currents in a metal object subjected to time varying magnetic fields.

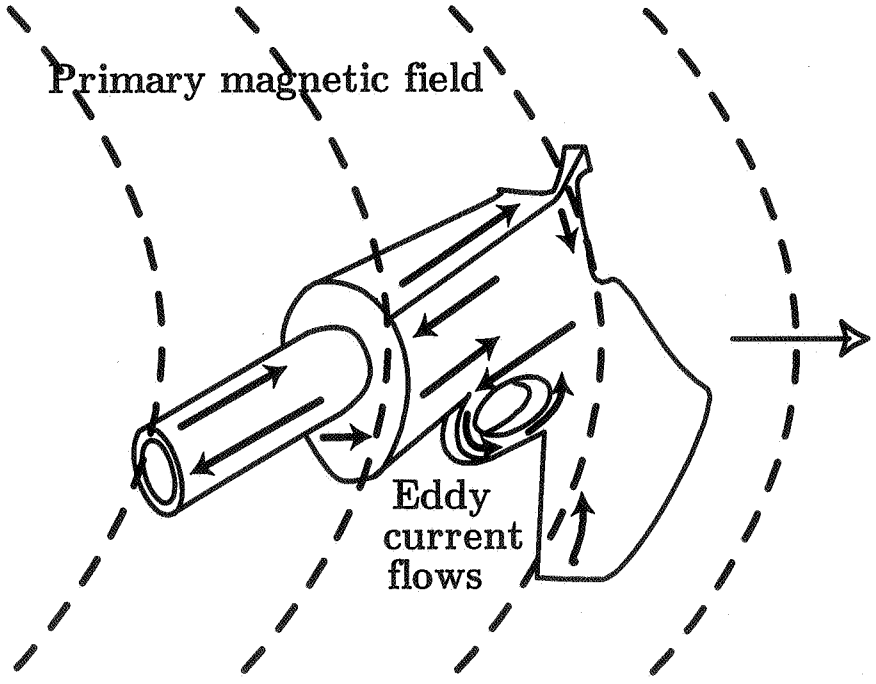

Figure 2. Approximate eddy currents on a handgun due to an incident variable magnetic field.

penetrate through the body.

The body consists of muscle, fat, bone, organs of various types of tissue, and cavities. All these materials can be treated as nonmagnetic. Since the dielectric properties of human tissues are heterogeneous and vary from tissue to tissue, we need to correctly simulate the electrical response of the particular area of the human body where the PMED is implanted. For metal detector research, we need to emphasize tissue conductivity, rather than permittivity, since skin depth and plane-wave impedance, in nonmagnetic conductive materials at low frequency, depend more strongly on the conductivity. At low frequencies the real part of the permittivity has little effect on the impedance. Gabriel and Gestblom have compiled extensive data on various human tissues and developed a database which reports measurements of various human tissues such as head, brain, muscle, fat, and bone [2].

Phantom materials studied by previous researchers are summarized in table 1 [3–11]. Previously developed phantoms have been based on liquids and salts, gelling agent and salts, carbon black mixtures with polymer resins. For example, Hagmann et al. used glycine, salt, and the gelling agent, agarose or carrageenan [5]. With this mixture, they found they could match permittivity and conductivities of the human body. Kato [8] used a mixture of agar, water, and salts that could be heated to a gel state. Kato found that the semi-solid material could be sculptured to produce a body shape, but degraded in time. Chou et al. [6] used a mixture of water, salts, and a gelling agent to form a semi-solid material. Andreuccetti [7] used a mixture of water, polyacrylamide, and salts to produce a semi-solid phantom. Marchal [10] used a mixture of water, salts, and gelatine to produce a stable phantom jelly-like material. The glycine- agarose-based materials need refrigeration. Most of the studies that dealt with low frequencies (1 kHz to 1 MHz) used liquid materials, while the studies that dealt with megahertz to gigahertz frequencies used semi-solid materials [9]. Liquids work well at low frequencies because the mobile ions from the salts mimic the tissue's dielectric-loss response. The standard method for Specific Absorption Rate (SAR) for wireless communication devices uses a liquid mixture of water, NaCl, alcohol, sugar, and other additives, depending on the frequency [11]. The IEEE Standard uses a mixture of water, NaCl, sugar, and couple other compounds (see the new IEEE Standard Method 1528-200x, in review at time of publication). These methods were developed to mimic human body properties in the low microwave range.

In our study we considered four candidate materials. These were potassium chloride solution (KCl), a liquid composed of a mixture of ethylene carbonate, propylene carbonate, and tetraethyleammonium tetrafluoroborate (TEATFB) [3], carbon black mixed into silicone rubber (CBS), and glycine, carrageenan, KCl, and water. All of these composites can be mixed to match the average conductivity of the human body tissues. There are advantages

Table 1. Previous work on human phantom materials.

Frequency	Materials	Citation and Date
1 Hz to 1 GHz	TEATFB	Broadhurst et al. 1987 [3]
900 MHz	graphite and resin	Kobayashi et al. 1993 [4]
10 to 100 MHz	glycine, NaCl	Hagmann et al. 1992 [5]
500 MHz to 3 GHz	silicone rubber, carbon black	Nikawa et al. 1996 [9]
200 MHz to 2.45 GHz	gel, aluminum powder, NaCl	Chou et al. 1984 [6]
750 MHz to 5 GHz	polyacrylamide, NaCl	Andreuccetti et al. 1988 [7]
5 to 40 MHz	agar, sodium azide, PVC powder	Kato et al. 1987 [8]
10 to 50 MHz	gelatine and NaCl	Marchal et al. 1989 [10]
300 MHz to 1 GHz	liquid	CENELEC Standard [11]

and disadvantages for each of these phantom materials for medical detectors (PMMDs). We concentrated the majority of our effort on understanding a semi-solid, CBS PMMD (for background on CBS see Appendices A and B). Semi-solid materials have several advantages over liquids. For example, CBS phantom composites are rubbery materials that allow test objects to be permanently embedded or encapsulated at a particular position.

3. Applications of Phantom Materials

The draft revisions of the National Institute of Justice (NIJ) standards for HH and WT metal detectors contain a body-cavity concealment test, which is intended to detect metal objects concealed within the human body cavities by use of human subjects. What is desired is a phantom material that can correctly simulate the EM properties of human body tissues over the frequency range at which metal detectors operate so that the body-cavity concealment test can be reproduced.

Electrical interference in medical implant devices is another area of concern in metal detectors. These devices are often studied by testing them when encapsulated in phantom materials. The types of medical electronic devices used to assist or supplant poor or absent physiological functions include, but are not limited to, cardiac defibrillators, hearing aids, cardiac pacemakers, infusion pumps, and spinal cord stimulators. PMEDs may be implanted within the body or located on the surface. Some PMEDs are programmed magnetically, and all may be susceptible to external electromagnetic energy radiated by other electronic or electrical devices. PMEDs are frequently exposed to electromagnetic interference (EMI)

emitted from other electronic devices. The interaction between PMEDs and intentional radiators is a major concern. Commonly encountered radiators include HH and WT metal detectors typically used for screening applications. These detectors emit frequencies close to those used by PMEDs, that could cause interference problems. Unfortunately, there is little information, other than anecdotal, about the interaction of PMEDs with HH and WT metal detectors. Since testing of PMEDs is often accomplished by encapsulating the device in phantom materials, we must characterize materials that have conductivities that are close to those of human tissues.

4. Conductivity of Materials

4.1 Electrical Properties of Conductive Materials

Electric and magnetic fields are attenuated as they travel through lossy materials. The skin depth δ is the distance a plane wave travels, where it is decreased in magnitude by $1/e$:

$$\delta = \frac{1}{\sqrt{\pi f \mu_0 \mu_r' \sigma}}. \tag{1}$$

In eq. (1), σ is the dc conductivity, μ_r' is the real part of the relative permeability, and f is the frequency. We see that the frequency, conductivity, and permeability of the material determine the skin depth. The higher the frequency, permeability, and conductivity, the smaller the skin depth [12].

The wavelength of an electromagnetic wave in a material is influenced by the permittivity and the wavelength in the material is $\lambda = c_{vac}/\sqrt{\epsilon_r'} f$, where c_{vac} is the speed of light in vacuum. The complex permittivity including the conductivity is defined as

$$\epsilon^* = \epsilon_r' \epsilon_0 - j(\epsilon_r'' \epsilon_0 + \frac{\sigma}{\omega}). \tag{2}$$

The presence of dc conduction produces a low-frequency loss σ/ω, in addition to polarization loss (ϵ_r''). When electromagnetic fields impinge on a metal surface, the wave is strongly attenuated and the surface resistance is

$$R_s = \frac{1}{\delta \sigma} = \sqrt{\frac{\pi f \mu_0 \mu_r'}{\sigma}}. \tag{3}$$

The surface resistance increases in proportion to the square root of the frequency. The impedance is a strong function of σ at low frequencies. If $Z = \sqrt{\mu^*/\epsilon^*} = \sqrt{i\omega\mu'/(j\omega\epsilon' + \sigma)}$ and $Z_0 = \sqrt{\mu_0/\epsilon_0}$ are plane-wave impedances, then the plane-wave reflection coefficient is

$$\Gamma_p = \frac{Z - Z_0}{Z + Z_0}. \tag{4}$$

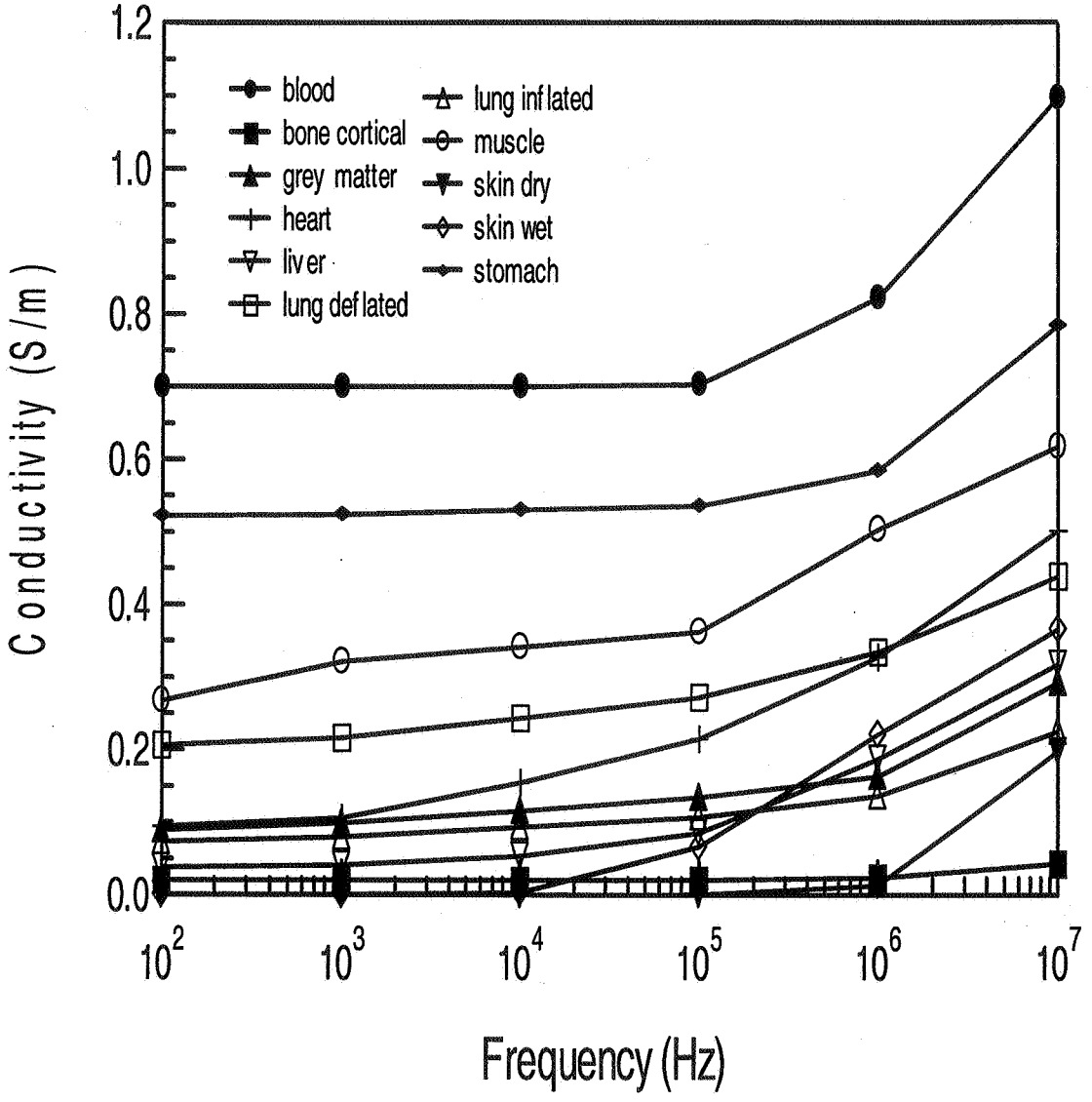

Figure 3. Measurements of the ac conductivity (S/m) on various body tissues by Gabriel [2] (no uncertainties assigned).

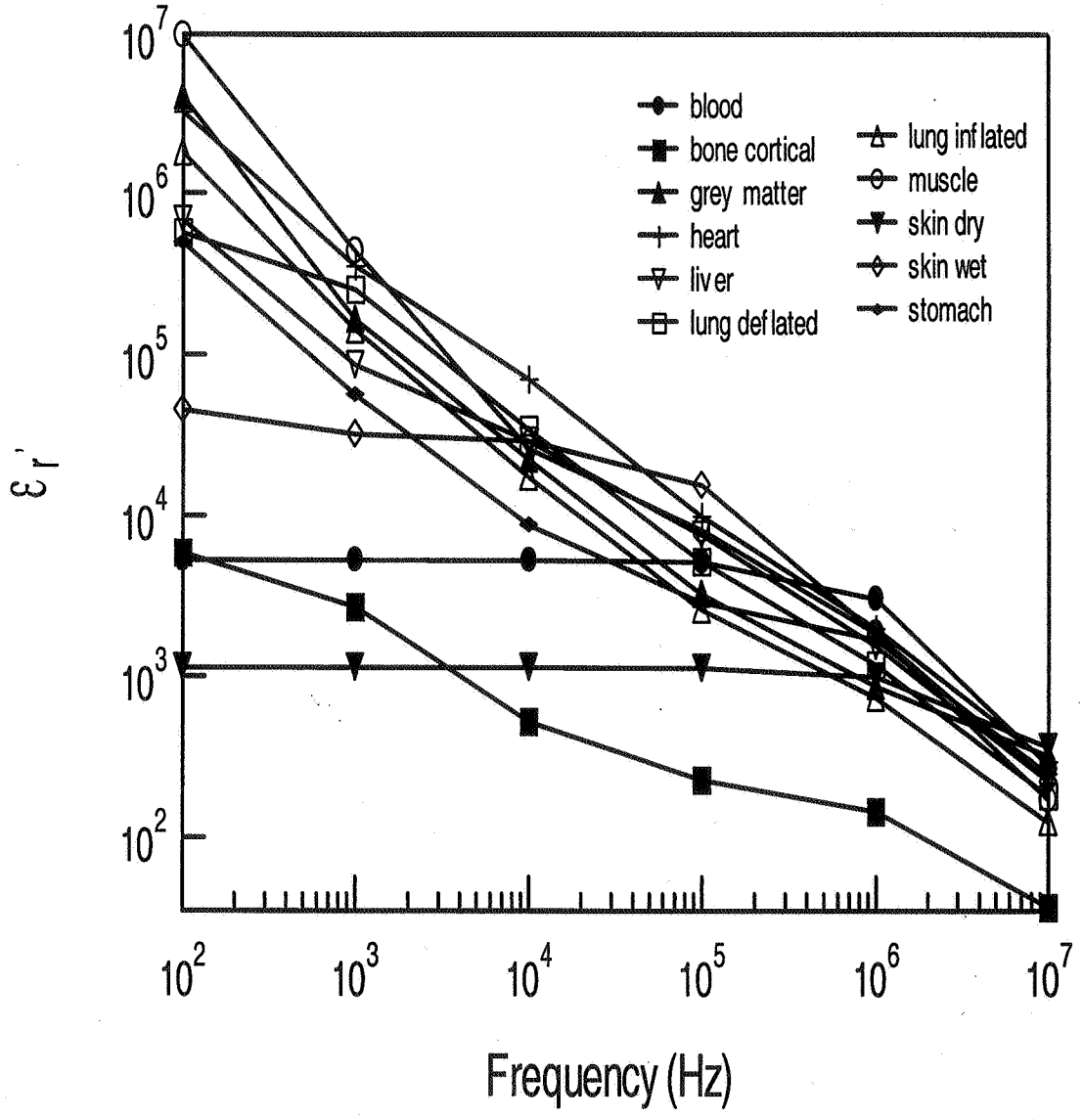

Figure 4. Measurements of relative permittivity (S/m) on various body tissues by Gabriel [2] (no uncertainties assigned).

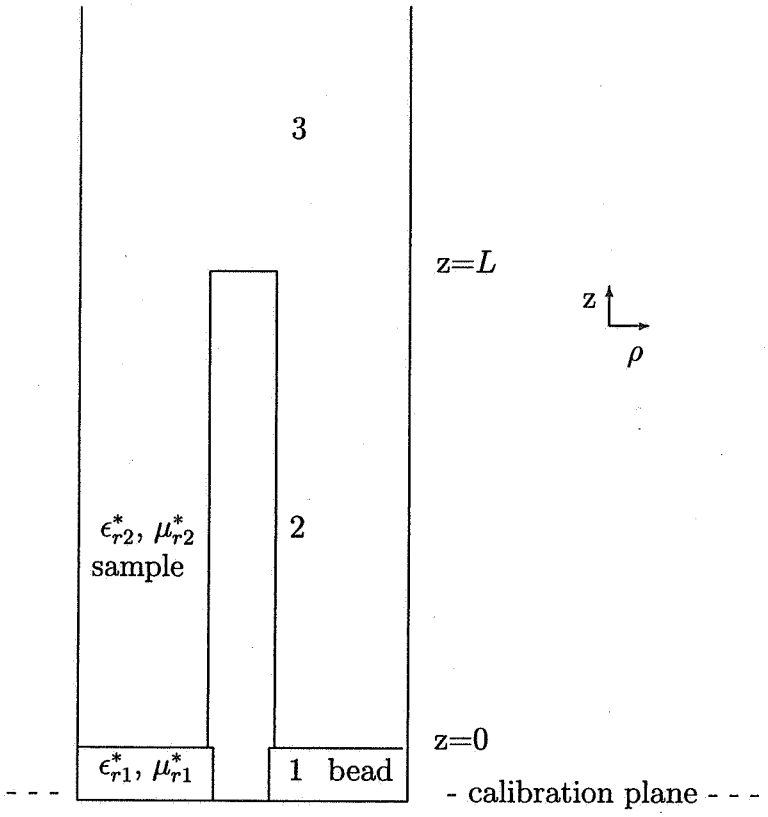

Figure 5. The shielded open-circuited sample holder for measurements of conductivity. The regions 1 through 3 are referred to in the full-mode model developed in the Appendix C.

4.2 Conductivity Measurements

The conductivities of CBS PMMDs were measured using an open-circuited coaxial holder depicted in figure 5. This fixture consists of an open-circuited 14 mm coaxial line with the center conductor shorter than the outer-conductor shield. We developed a full-mode model for the open-circuit termination (see Appendix C). This model includes a rigorous treatment of the fringing capacitance at the open-circuit termination. The measurement data are the reflection coefficient, Γ, from a network analyzer or C and G from a LCR meter. As a check of our model we measured liquid KCl reference standards.

4.3 Variable-Temperature Measurements

The temperature system we used was an environmental chamber that operates from -150 °C to 150 °C [13]. The chamber has feed-through bulkhead adapters on the sides for passage of coaxial feeds for cavities or transmission lines. The chamber has purging ports for applying nitrogen gas to reduce oxidation and content of water vapor.

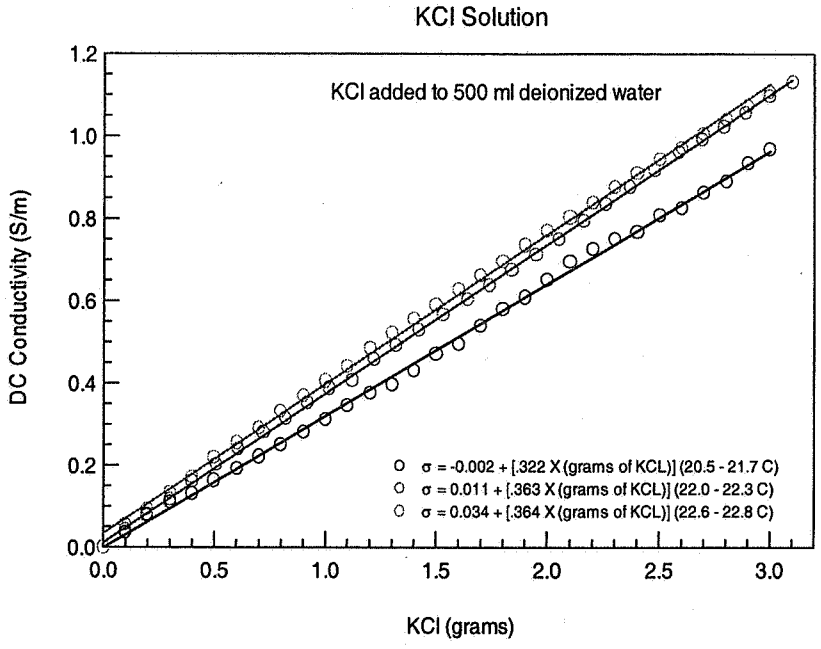

Figure 6. Conductivity of potassium chloride solution. Also shown are regression fits for the conductivity as a function of concentration of KCl and for different temperatures.

4.4 Conductivity of Candidate Liquids

In this section we summarize the measurements on liquid PMMDs. We will present results on the concentration and temperature dependence of the conductivity. For the measurements on liquids we used both a dc conductivity probe and a shielded open-circuited holder. In figure 6, the dc conductivity of KCl in 500 ml deionized water is plotted versus KCl concentration for minor variations in temperature. The uncertainties in the liquid measurement are due to uncertainties in the measurement device and uncertainties in the chamber temperature. Our lab has a temperature stability of ± 2 °C. For measured conductivities of $\sigma = 0.5$ (S/m), the Type B expanded relative uncertainty was $U = ku_c = 0.02$ (k-2).

For the KCl solution the dependence of conductivity on KCl concentration is nearly linear. We see that we can obtain the required conductivities using the appropriate concentration of KCl. We also studied the temperature dependence and time stability of these solutions and the results are shown in figures 7 and 8 for temperature of 22 °C $\pm$ 0.5 °C. The fluctuations in figure 8 are due to temperature variations when calibrating the conductivity probe. For comparison, typical conductivities and permittivities of the human body were shown in figures 3 and 4. There is no percolation threshold for these materials.

The following formula fits the conductivity of a mixture in (S/m) of deionized water as a function of KCl content at 22 °C, where m_{kcl} is the mass per milliliter of the potassium

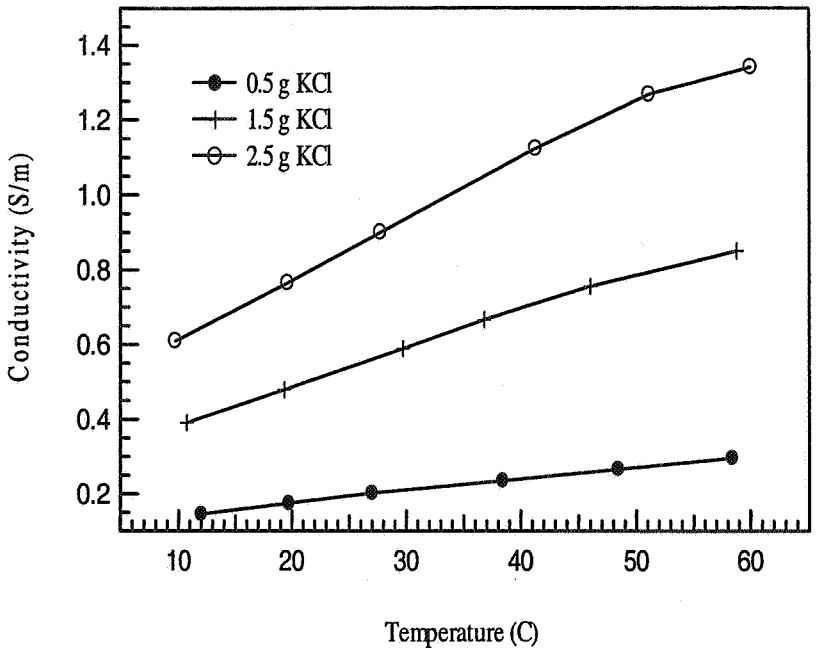

Figure 7. Temperature dependence of conductivity of the potassium chloride solution.

chloride,

$$\sigma = 0.011 + 181.5\ m_{kcl}. \tag{5}$$

We also measured another liquid mixture that was studied by Broadhurst [3]. The results are shown in figure 9. This liquid contains a 50-50 mix of ethylene carbonate and propylene carbonate and the salt tetraethyleammonium tetrafluoroborate (TEATFB). We found that by varying the salt concentration we could vary the conductivity in the desired range. A measurement of the mixture given in figure 9. The following formula fits the conductivity data as a function grams of TEATFB (m_{tea}) per 100 g of propylene carbonate

$$\sigma = 0.0095 + .0725 m_{tea} - 0.00112 m_{tea}^2. \tag{6}$$

We also studied the temperature and time stability of these solutions and the results are shown in figures 10 and 11.

4.5 Conductivities of Carbon-Black-Silicone Materials

We studied two types of CBS (a silicone rubber composite) mixtures. These were 'XC-72' and 'Black Pearls', both from Cabot Inc.[1] The conductivity of CBS is not a linear function

[1]Products or companies named here are cited only in the interest of complete scientific description, and neither constitute nor imply endorsement by the National Institute of Standards and Technology or by the U.S. Government. Other products may be found to serve just as well.

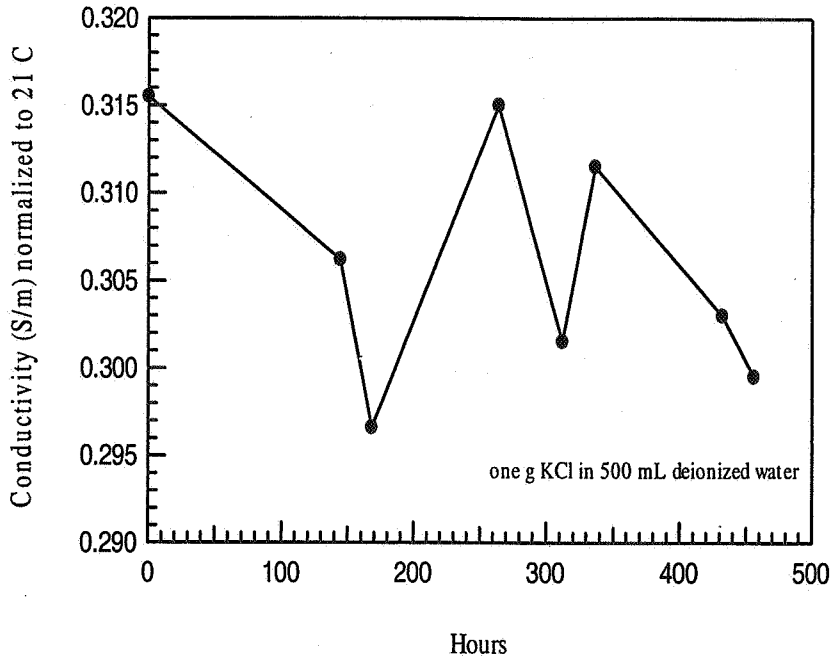

Figure 8. Time stability of the potassium-chloride solution conductivity normalized to the measurement at 21 °C. Note: Fluctuations are due primarily to temperature variations.

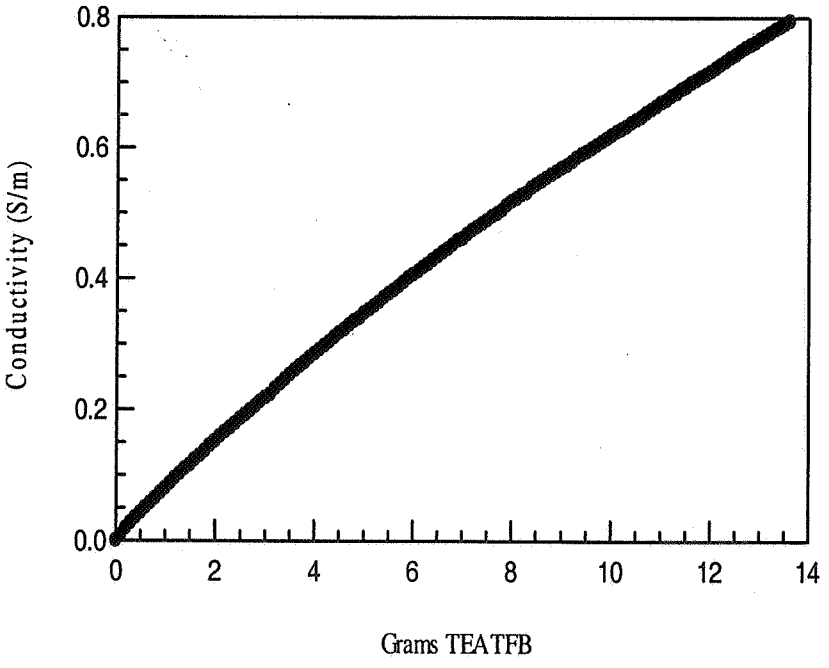

Figure 9. TEATFB solution with 100 ml propylene carbonate and 125 g ethylene carbonate.

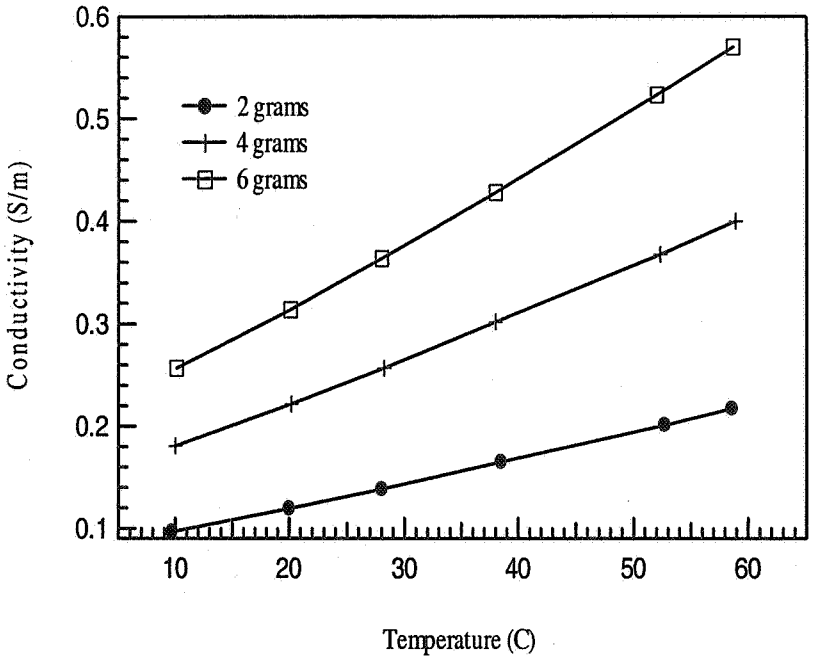

Figure 10. Temperature dependence of the conductivity for various concentrations of the salt for TEATFB with 100 ml propylene carbonate and 125 g ethylene carbonate and varying salt concentrations.

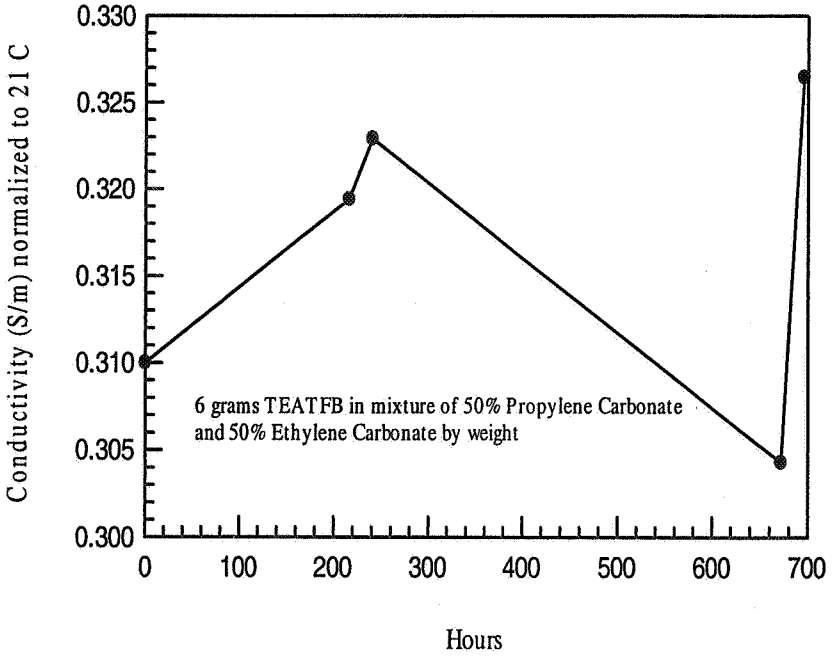

Figure 11. Time stability of the conductivity of 6 g TEATFB with 100 ml propylene carbonate and 125 g ethylene carbonate. The temperature uncertainty over the measurement was $\pm 1°C$.

of concentration, as was the case with KCl. The CBS conductivity goes through a percolation threshold where it abruptly increases. This percolation phenomena has been studied previously [14–16]. In figures 12 through 22 we display conductivities of CBS composites. The measurements of the composite, as a function of carbon-black-silicone weight fractions, showed that we could also simulate human-body conductivity with carbon-black, 'XC-72' and 'Black Pearls'. As the concentration increased to 20 % for 'XC-72' carbon black and to 10 % for the 'Black Pearls', the CBS became very difficult to mix. The percolation threshold occurs between 10 % to 15 % carbon black by weight for the 'XC-72' material and between 6 % to 8 % by weight for the 'Black Pearls' mixture. We determined that with CBS conductivity of $\sigma = 0.001$ (S/m), the Type B expanded relative uncertainty was $U = ku_c = 0.001$ (k-2); with $\sigma = 0.1$ (S/m), the Type B expanded relative uncertainty was $U = ku_c = 0.02$ (k-2); and with $\sigma = 0.56(S/m)$, the Type B expanded relative uncertainty was $U = ku_c = 0.02$ (k-2). The density of carbon black is about 1.8 g/ml. Therefore conversion between weight fraction and volume fraction is accomplished by multiplying by 1.8.

We performed tests that study the concentration dependence and reproducibility of the mixtures. In figure 12, we plot the conductivity versus frequency as a function of the weight fraction of carbon black 'XC-72' in silicone. The conductivity increases abruptly near 12 % carbon-black concentration for the 'XC-72' mixture. This conductivity increase is due to a percolation phenomenon, where electronic tunneling transport connect the conducting paths throughout the sample [16]. The measurements on different batches as a function of curing time indicates the degree of reproducibility with the mixing process we used as shown in figures 12 through 16. We see that the average conductivity varies exponentially with concentration of 'XC-72' carbon black as shown in figure (12) for 'XC-72' and in figure (16) for 'Black Pearls' (see Appendix D). Above the percolation threshold it varies nearly linearly with concentration. The conductivity stabilized after temperature annealing at a temperature of 60 °C for 2 h, as shown in figures 19 and 20. See Appendix D for a review of conductivity of mixtures.

The time drift in the measurement is given in figures 19 and 20 by the "box" symbols. The temperature dependence is given figures 21 and 22. The initial increase in conductivity as temperature increases we attribute to relaxation and curing of the composite.

4.6 Glycine-Based Phantom Material

We also studied a mixture of glycine, carrageenan, KCl, and water. The results are shown in figures 23 and 24. The carrageenan causes the glycine solution to gel to a jelly-like consistency, depending on water content. The resultant mixture requires refrigeration. Most of the measurements on this solution were made with a dc-conductivity meter. However, a

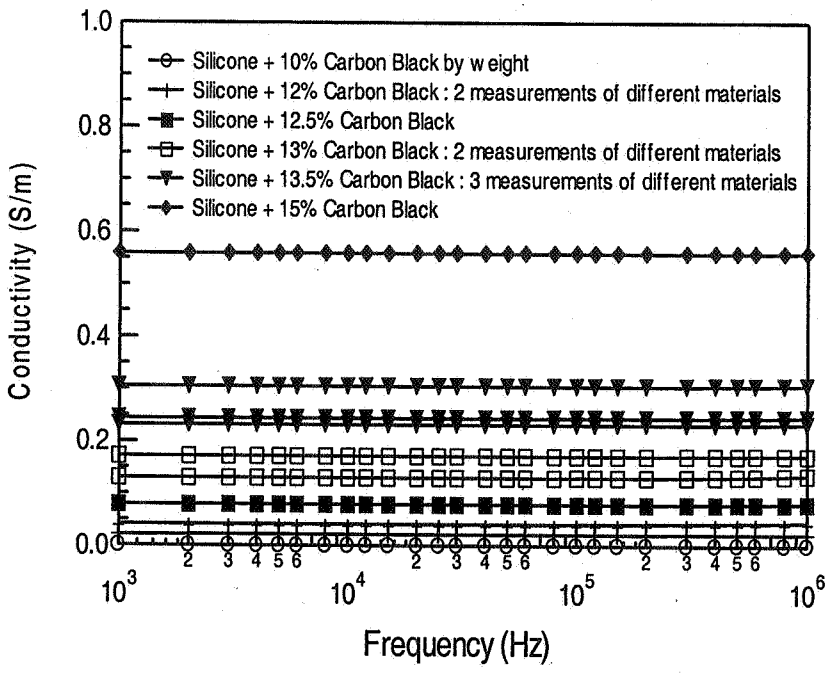

Figure 12. CBS using 'XC-72'.

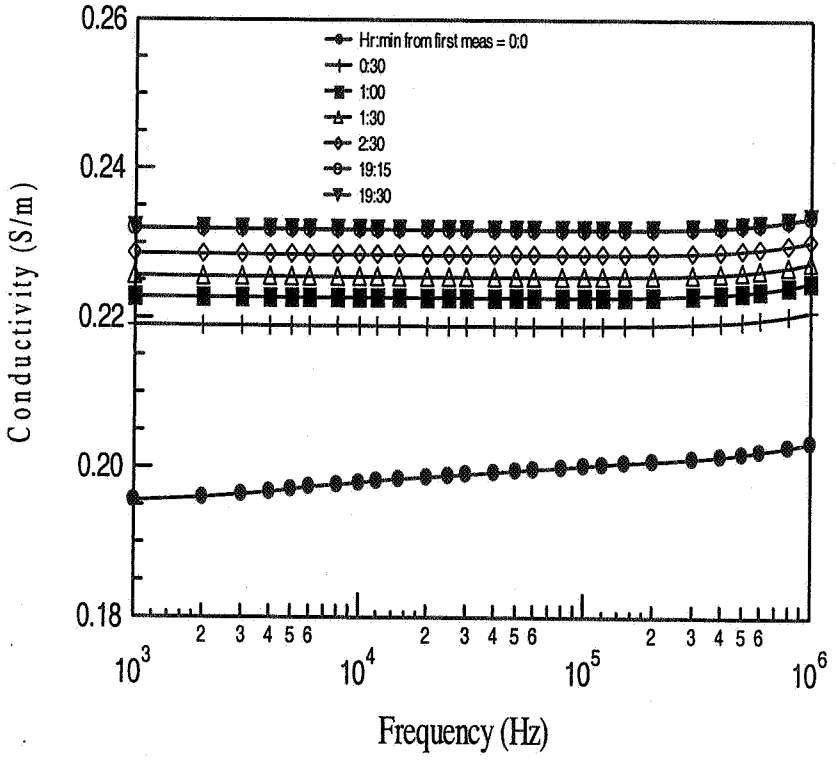

Figure 13. Conductivity changes in time due to curing and relaxation for 13.5 % CBS 'XC-72' mixture, sample 1.

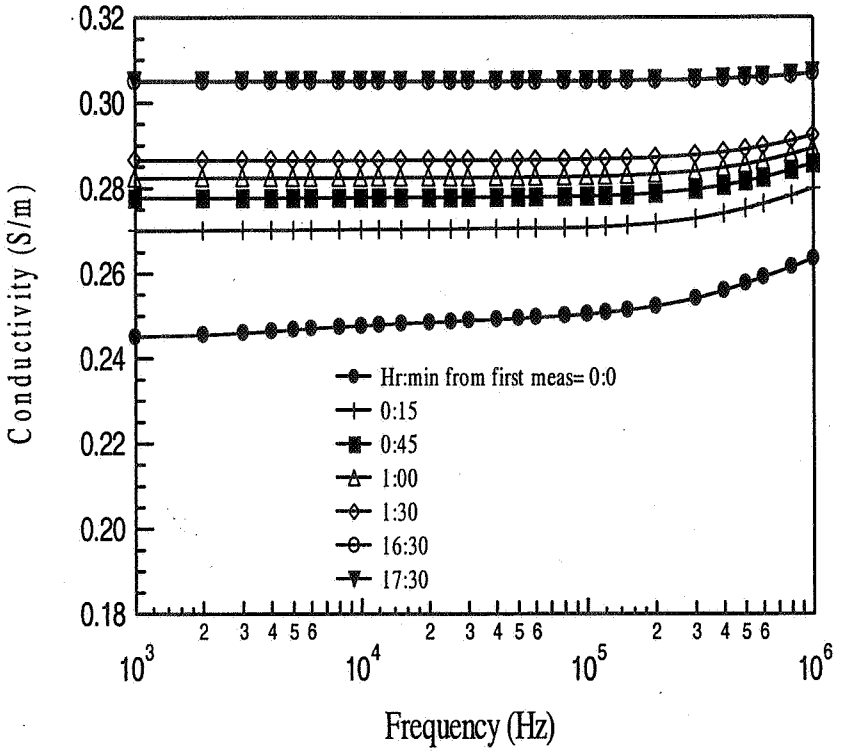

Figure 14. Conductivity changes with time due to curing and relaxation in the 13.5 % CBS 'XC-72' mixture, sample 2.

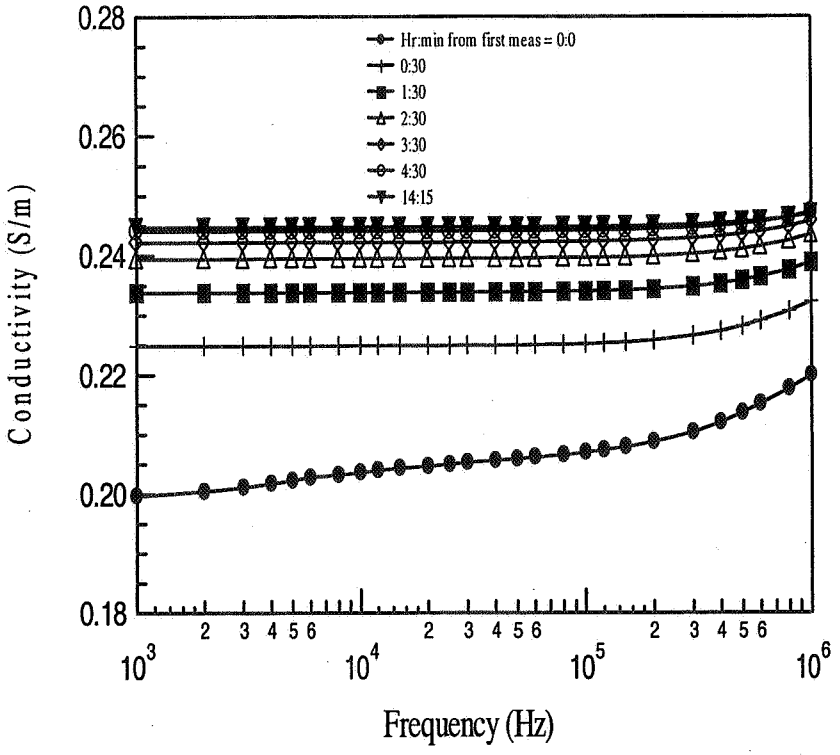

Figure 15. Conductivity changes in time due to curing and relaxation for 13.5 % CBS 'XC-72', sample 3.

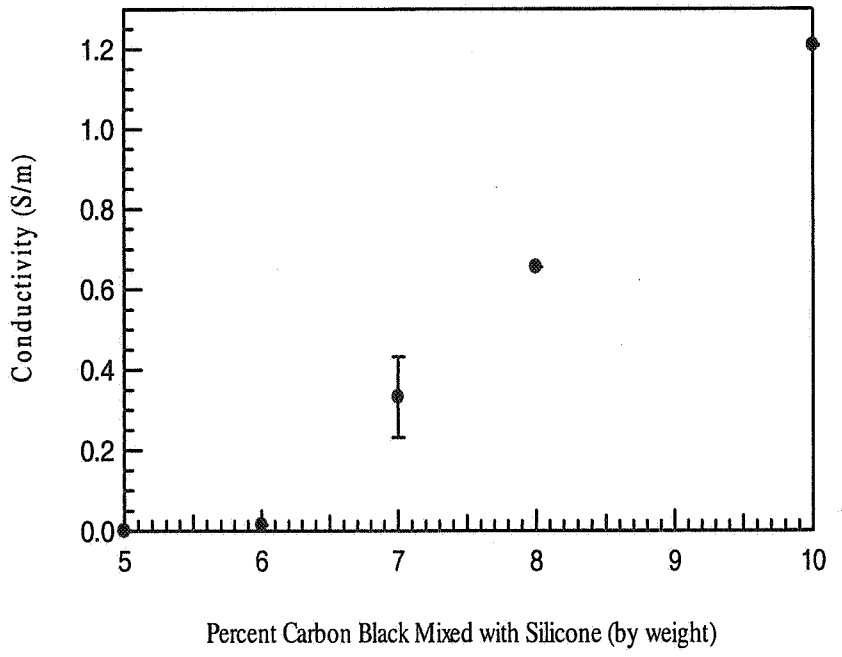

Figure 16. Conductivity as a function of carbon-black concentration for 'Black Pearls' mixture.

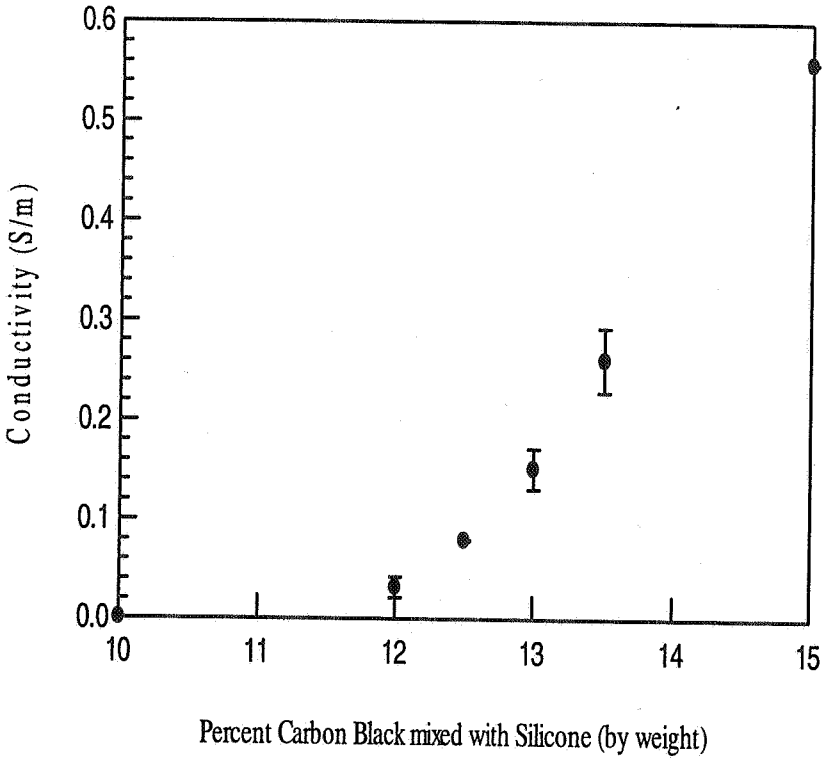

Figure 17. Conductivity as a function of carbon-black concentration for 'XC-72' mixture.

test was also performed to compare the dc-conductivity results to those from the frequency-dependent shielded open-circuit holder. The measurements at 100 kHz are shown in figure 24.

5. Discussion

Conductivities close to those of tissues in the human body can be reproduced by either carbon-black composites, glycine composites, or various salty solutions. The liquids can be easily mixed to obtain the desired response. These liquids also show good time stability in the conductivity and a predictable temperature response. The CBS shows less time stability. To obtain time stability in the CBS the sample must be temperature annealed. The conductivity of CBS exhibits a percolation threshold at which conductivity increases abruptly. The temperature dependence in the CBS is more complicated than that of liquids and depends on whether the sample's carbon-black concentration is above or below the percolation threshold. The silicone material has the advantage of being more rugged than the glycine and liquid mixtures. CBS has the disadvantage that its curve for conductivity versus concentration is very steep around the percolation threshold. Liquids are not as

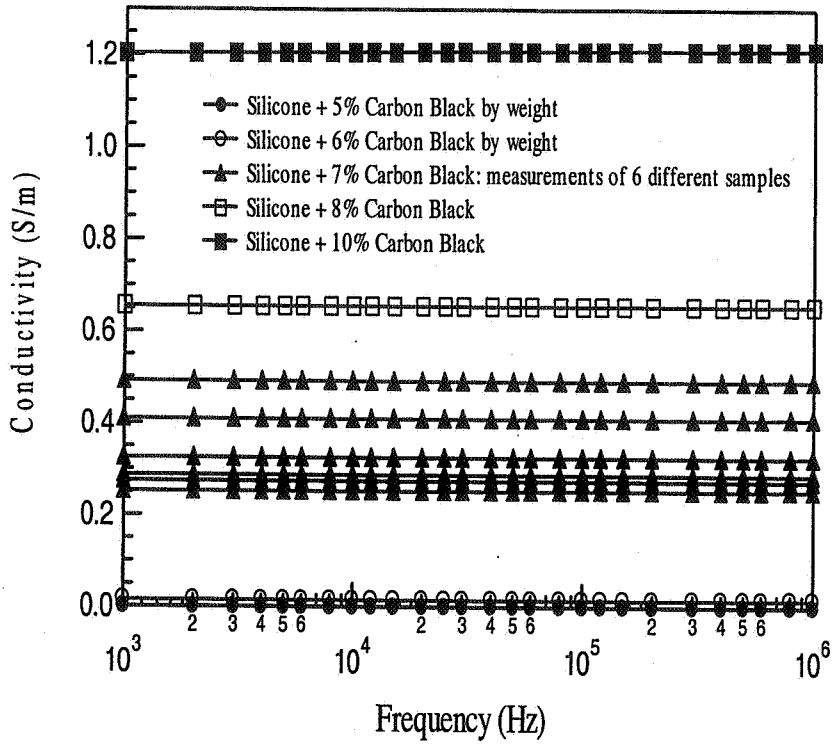

Figure 18. Conductivity as a function of carbon-black concentration for 'Black Pearls' mixture.

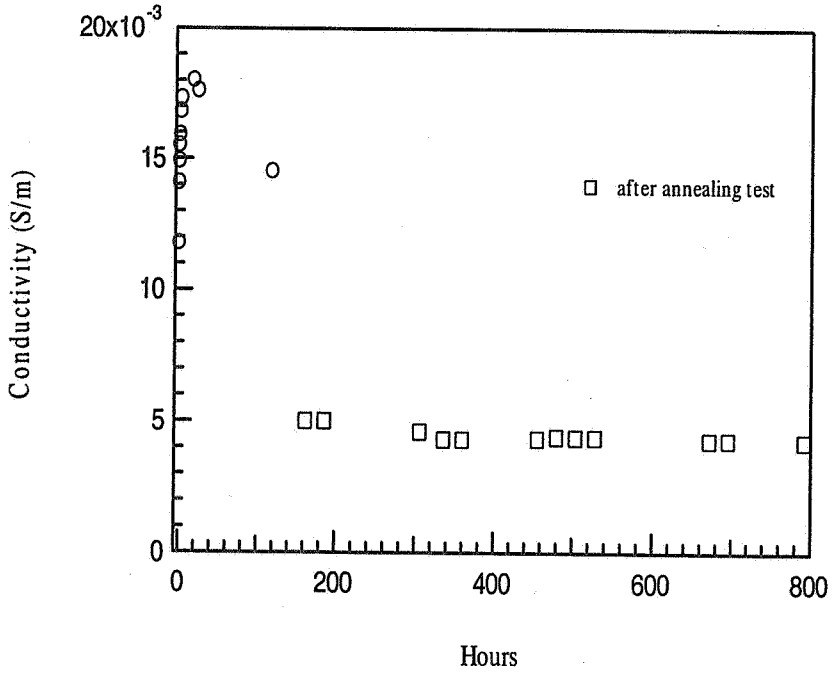

Figure 19. Change in conductivity due to relaxation in 6 % 'Black Pearls' CBS.

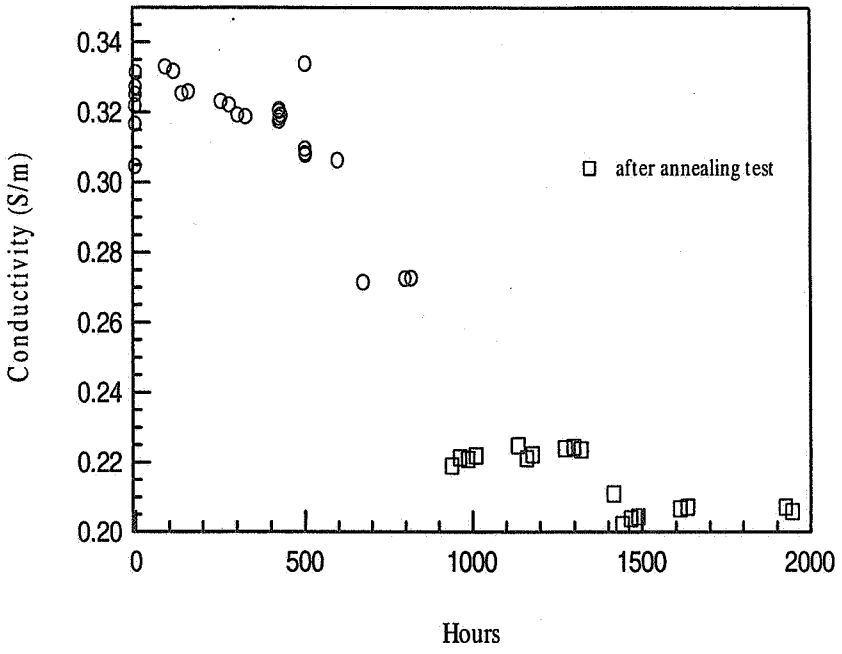

Figure 20. Change in conductivity due to relaxation in 7 % 'Black Pearls' CBS.

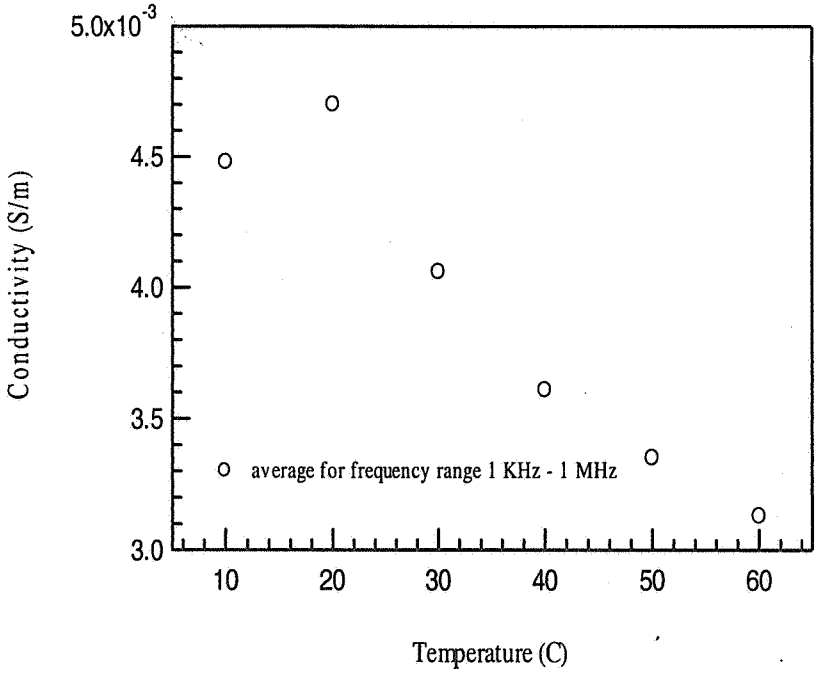

Figure 21. Dependence on temperature of 6 % by weight 'Black Pearls' CBS.

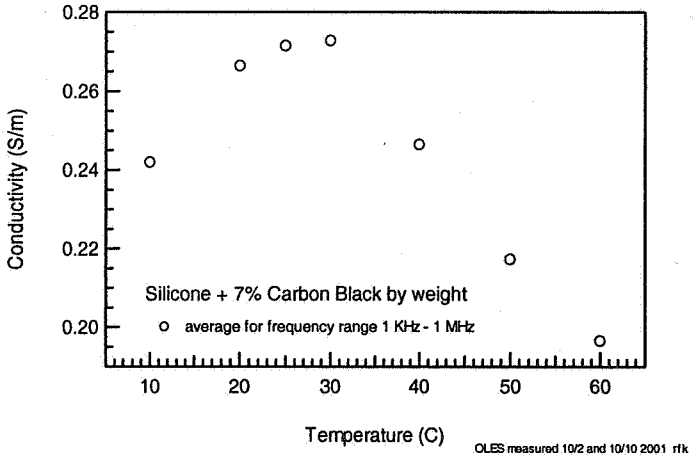

Figure 22. Dependence on temperature of 7 % by weight CBS 'Black Pearls' CBS.

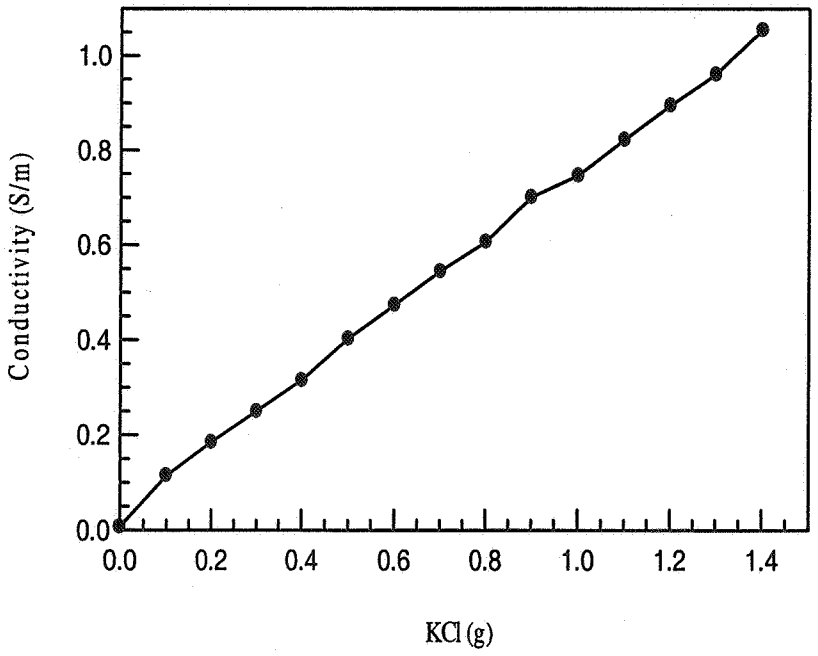

Figure 23. The conductivity of 6 % by weight glycine in water, with carrageenan as a function of KCl concentration.

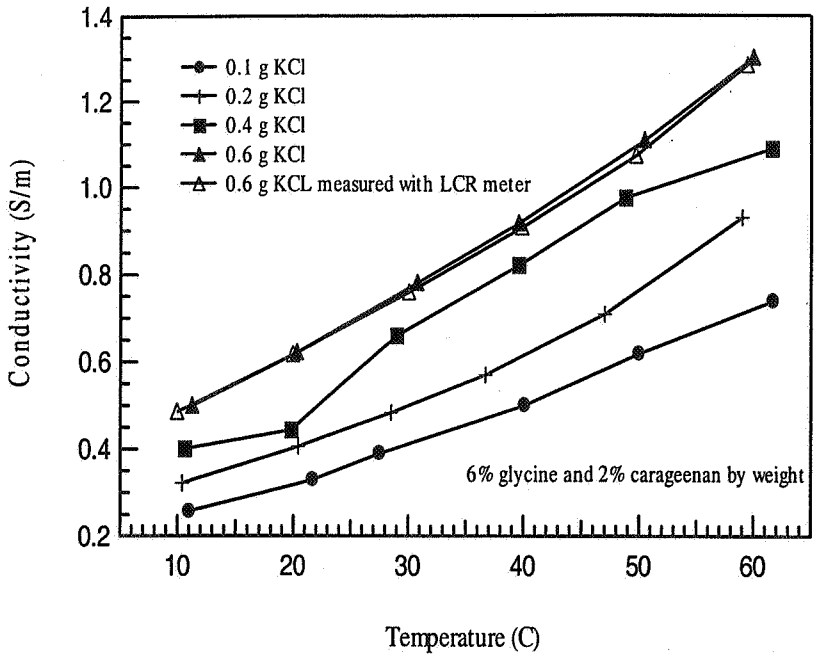

Figure 24. The conductivity of 6 % by weight glycine in water, with carrageenan as a function of temperature and KCl concentration.

convenient as solids for research materials for use with metal detectors.

We acknowledge the support of the National Institute of Justice and Dr. George Lieberman and Kathy Higgins of the Office of Law Enforcement Standards of NIST. We acknowledge Les Burk of Ranger Security Detectors for helpful conversations and permission to reproduce figures of metal detectors and magnetic fields found on their web site.

6. References

[1] K. L. Stricklett and J. Baker-Jarvis, "Electrical properties of biological materials: A bibliographic survey," NISTIR 6564, Natl. Inst. Stand. Technol., 2001.

[2] C. Gabriel and B. Gestblom, "Microwave absorption in aqueous solutions," *Nature*, vol. 328, pp. 145–146, 1987.

[3] M. G. Broadhurst, C. K. Chiang, and G. T. Davis, "Dielectric phantoms for electromagnetic radiation," *J. Mole. Solids*, vol. 36, pp. 47–64, 1987.

[4] T. Kobayashi, T. Nojima, K. Yamada, and S. Uebayashi, "Dry phantom composed of ceramics and its application to SAR estimation," *IEEE Trans. Microwave Theory Techn.*, vol. 41, pp. 136–140, 1993.

[5] M. J. Hagmann, R. Calloway, A. Osborn, , and K. Foster, "Muscle equivalent phantom materials for 10-100 MHz," *IEEE Trans. Microwave Theory Techniques*, vol. 40, pp. 760–762, 1992.

[6] C. Chou, G. Chen, A. Guy, and K. Luk, "Formulas for preparing phantom muscle tissue for various radiofrequencies," *Bioelectromagn.*, vol. 5, pp. 435–441, 1984.

[7] D. Andreuccetti, M. Bini, and A. Ignesti, "Use of polyacrylamide as a tissue-equivalent material in the microwave range," *IEEE Trans. Biomed. Eng.*, vol. 35, pp. 275–277, 1988.

[8] H. Kato and T. Ishida, "Development of an agar phantom adaptable for simulation of various tissues in the range 5-40 MHz," *Phys. Med. Bio.*, vol. 32, pp. 221–226, 1987.

[9] Y. Nikawa, M. Chino, and K. Kikuchi, "Soft and dry phantom modeling material using silicone rubber with carbon fiber," *IEEE Trans. Microwave Theory Techn.*, vol. 44, pp. 1949–1953, 1996.

[10] C. Marchal, M. Nadi, A. J. Tosser, C. Roussey, and M. L. Gaulard, "Dielectric properties of gelatine phantoms used for simulations of biological tissues between 10 and 50 MHz," *Int. J. Hyperthermia*, vol. 5, no. 6, pp. 725–732, 1989.

[11] "CENELEC Standard 50361: Basic standard for the measurement of the Specific Absorption Rate related to human exposure to electromagnetic fields from mobile phones (300 MHz - 3 GHz)" *CENELEC*, 2000.

[12] M. J. Peters, J. G. Stinstra, and M. Hendriks, "Estimation of the electrical conductivity of human tissue," *Electromagn.*, vol. 21, pp. 545–557, 2001.

[13] J. Baker-Jarvis and J. H. Grosvenor, "Dielectric and magnetic measurements from -50c to 200 c and in the frequency band 50 MHz to 2 GHz," Tech. Rep. NISTIR 5045, Natl. Inst. Stand. Technol., 1996.

[14] E. Tuncer and S. M. Gubanski, "Electrical properties of filled silicone rubber," *J. Phys. Condens. Matter*, vol. 12, pp. 1873–1897, 2000.

[15] A. Nakayama, M. Inagaki, M. Miyauchi, and N. Itoh, "Dielectric dispersion of polycrystalline aluminum nitride at microwave frequencies," *J. Am. Ceram. Soc.*, vol. 79, pp. 1453–1456, 1996.

[16] S. Nakamura, T. Tomimura, and G. Sawa, "Electrical conduction mechanism of polymer carbon black composites below and above the percolation threshold," in *Proc. Electrical Insulation and Dielectric Phenomena*, vol. 1, pp. 265–268, IEEE, 1998.

[17] L. Hartshorn and W. H. Ward, "The measurement of the permittivity and power factor of dielectrics at frequencies 10^4 to 10^8 cycles per second," *J. Inst. Elec. Eng.*, vol. 79, pp. 597–609, 1936.

[18] A. von Hippel, *Dielectric Materials and Applications.* Cambridge, MA: M.I.T. Press, 1954.

[19] H. E. Bussey, "Dielectric measurements in a shielded open circuit coaxial line," *IEEE Trans. Instrum. Meas.*, vol. IM-29, pp. 120–124, June 1980.

[20] J. Baker-Jarvis, M. D. Janezic, and C. A. Jones, "Shielded open-circuited sample holder for dielectric measurements of solids and liquids," *IEEE Trans. Instrum. Meas.*, vol. 47, pp. 338–344, April 1998.

[21] S. Jenkins, T. E. Hodgetts, R. N. Clarke, and A. W. Preece, "Dielectric measurements on reference liquids using automatic network analyzers and calculable geometries," *Meas. Sci. Tech.*, vol. 1, pp. 691–702, 1990.

[22] P. I. Somlo, "The discontinuity capacitance and the effective position of a shielded open circuit in a coaxial line," *Proc. Inst. Radio Elec. Eng. Australia*, vol. 28, pp. 7–9, January 1967.

[23] W. R. Scott and G. S. Smith, "Error analysis for dielectric spectroscopy using shielded open-circuited coaxial lines of general length," *IEEE Trans. Instrum. Meas.*, vol. IM-35, pp. 130–137, June 1986.

[24] P. N. Hill and H. E. Green, "*In situ* measurement of soil permittivity and permeability," *J. Electrical Electronics Eng., Australia*, vol. 2, pp. 205–209, December 1982.

[25] R. L. Jesch, "Dielectric measurements of oil shales as functions of temperature and frequency," *IEEE Trans. Geosci. Remote Sensing*, vol. GE-22, pp. 99–105, March 1984.

[26] M. A. Stuchly and S. S. Stuchly, "Coaxial line reflection methods for measuring dielectric properties of biological substances at radio and microwave frequencies-A review," *IEEE Trans. Instrum. Meas.*, vol. IM-29, pp. 176–183, 1980.

[27] J. R. Mosig, J.-C. E. Besson, M. GE-Fabry, and F. E. Gardiol, "Reflection of an open-ended coaxial line and application to non-destructive measurement of materials," *IEEE Trans. Instrum. Meas.*, vol. 30, no. 1, pp. 46–51, 1981.

[28] H. Levine and C. H. Papas, "Theory of the circular diffraction antenna," *J. Appl. Phys.*, vol. 22, pp. 29–43, January 1951.

[29] D. S. McLachlan, "Analytical functions for the dc and ac conductivity of conductor-insulation composites," *J. Electroceramics*, vol. 52, pp. 93–110, 2000.

7. Appendix A: How Carbon Black is Produced

Carbon black is formed from heating hydrocarbons in a furnace as shown in figure 25. The reaction follows

$$C_xH_y + O_2 \rightarrow C + CH_4 + CO + H_2 + CO_2 + H_2O. \tag{7}$$

Carbon black is a particulate form of elemental carbon. In the carbon formation process, the liquid feedstock decomposes to form carbon radicals and condenses into spherical particles. The average diameter of the primary particles is between 12 nm to 75 nm. Therefore these are nanomaterials. The surface areas are between 25 m^2/g to 500 m^2/g. The primary particles collide in the reactor to form aggregates. The aggregates coalesce into larger particles called agglomerates, as shown in figure 26. The aggregates are held together by weak intermolecular forces. Carbon black has a density of approximately 0.16 g/cc. The smaller the size of the carbon-black particles, the higher the conductivity. The higher electrical conductivity is due to the interconnectedness of the aggregates. The size distribution of the carbon black changes when mixed, due to break up of conglomerates. The degree of breakup slightly changes the conductivity from batch to batch. In order to enhance reproducibility of the electrical conductivity, the materials must be mixed in a reproducible fashion.

Carbon-black polymer composites have a resistive relaxation due to motion of the polymer chains, which allows some reorganization of the carbon black with time. This manifests itself in a small drift in conductivity until the cure is complete. Literature sources recommend heating the cured sample (or annealing) to minimize resistive relaxation.

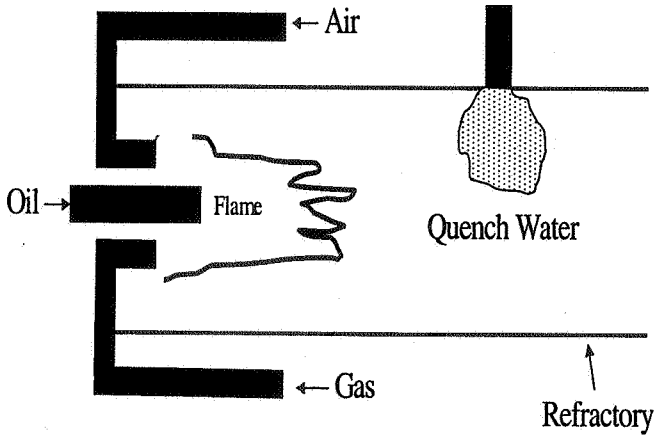

Figure 25. Carbon black manufacturing process.

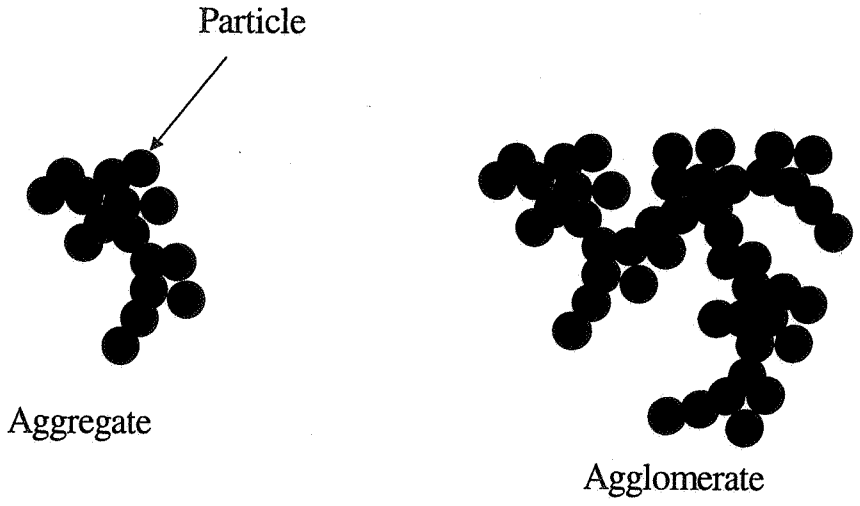

Figure 26. Carbon-black formation.

8. Appendix B: Percolation Threshold for Conductivity

When carbon black is added in a matrix material, a transition occurs from an insulating to conductive material as the volume fraction of carbon black increases. Percolation occurs when conducting paths are formed across the sample. Near the percolation threshold, the conductivity increases rapidly. The relaxation processes are dominated by tunneling processes that are strongly temperature dependent. Resistive relaxation is influenced by the application of static bias electric fields. This field-dependent effect is related to local dielectric breakdown and charge hopping over reduced potential barriers. Above the percolation threshold, the conduction is dominated by charge hopping.

9. Appendix C: Shielded Open-Circuited Holder

9.1 Measurements with the Shielded Open-Circuited Holder

The shielded open-circuited holder is very useful for measuring the dielectric properties of powders, liquids, and semisolids because of the ease of sample insertion. Previous work performed using the shielded open circuit at microwave frequencies has been performed by Hartshorn and Ward [17], Von Hippel [18], Bussey [19], Baker-Jarvis [20], and others [21–23]. Also Hill and Green [24] studied *in situ* measurements of soils using open-circuited transmission lines. Jesch [25] used the shielded open-circuited holder for measurements on oil shale. Biological tissues have been measured using the shielded open-circuited line, for example, by Stuchly and Stuchly [26].

9.2 Theoretical Formulation

Permittivity measurements are most accurate when the sample is located in a region of strong electric field. A strong electric field in a coaxial line is obtained most easily by use of a shielded open circuit. The shield on the open circuit allows an accurate analytical field model to be developed since the fields can be expanded into a series of discrete eigenmodes.

Consider a sample in the transmission line shown in figure 5. The shielded open-circuited holder consists of three sections. Region 1 is the bead in the airline, region 2 is the sample, region 3 is the shield region. The problem is to accurately characterize the shielded open circuit. We will develop a compact expression for the reflection coefficient in terms of air line and sample parameters.

We assume a time dependence of $\exp(j\omega t)$ in the coaxial line. Due to azimuthal symmetry, we need to consider only TEM and TM_{0mn} modes. We also assume that an incident TEM wave travels from the input port in the direction of the sample. At the sample discontinuity the TM_{0mn} modes are reflected, and a TEM wave and evanescent TM_{0mn} waves travel into the material. The problem we wish to solve is to relate the reflection coefficient to the complex permittivity.

The TEM mode admittance and reflection coefficient are related by

$$\Gamma_0 = \frac{Y_0 - Y}{Y_0 + Y}, \tag{8}$$

where Y_0 is the admittance of the air-filled line and Y is the admittance with the sample in the line.

The radial component of the electric fields in regions 1 through 3 are

$$E_{\rho(1)} = R_0(\rho)\exp(-\gamma_{10}z) + \sum_{n=0}^{\infty}\Gamma_n R_n(\rho)\exp(\gamma_{1n}z), \tag{9}$$

$$E_{\rho(2)} = \sum_{n=0}^{\infty} A_n R_n(\rho)\exp(-\gamma_{2n}z) + \sum_{n=0}^{\infty} B_n R_n(\rho)\exp(\gamma_{2n}z), \tag{10}$$

$$E_{\rho(3)} = \sum_{n=1}^{\infty} Q_n G_n(\rho)\exp(-\gamma_{3n}(z-L)), \tag{11}$$

where

$$\gamma_{i0} = j\frac{\omega\sqrt{\epsilon_{ri}}}{c}, \tag{12}$$

for $n = 0$, for $i = 1, 2$, and if $n > 0$

$$\gamma_{in} = j\sqrt{\epsilon_{ri}\mu_{ri}\frac{\omega^2}{c_{lab}^2} - k_{in}^2}, \tag{13}$$

for $i = 1, 2$ and for all modes in region 3. If the argument is negative (evanescent wave) then

$$\gamma_{in} = \sqrt{k_{in}^2 - \epsilon_{ri}\mu_{ri}\frac{\omega^2}{c_{lab}^2}}. \tag{14}$$

Here G_n are normalized eiegnfunctions in the cylindrical waveguide and R_n are the normalized eigenfunctions in the coaxial line, where

$$G_n(\rho) = S_n J_1(k_{3n}\rho). \tag{15}$$

The eigenvalues are found from the vanishing of the tangential electric field on the side wall

$$J_0(k_{3n}b) = 0. \tag{16}$$

Therefore $k_{3n} = p_n/b$, where p_n is the nth root of $J_0(x) = 0$, for $n = 0, 1, 2...$.

The azimuthal magnetic fields in regions 1 through 3 are

$$H_{\phi(1)} = \frac{j\omega\epsilon_1}{\gamma_{10}} R_0(\rho) \exp(-\gamma_{10} z) - \sum_{n=0}^{\infty} \Gamma_n \frac{j\omega\epsilon_1}{\gamma_{1n}} R_n(\rho) \exp(\gamma_{1n} z), \tag{17}$$

$$H_{\phi(2)} = \sum_{n=0}^{\infty} \frac{j\omega\epsilon_2}{\gamma_{2n}} A_n R_n(\rho) \exp(-\gamma_{2n} z) - \sum_{n=0}^{\infty} \frac{j\omega\epsilon_2}{\gamma_{2n}} B_n R_n(\rho) \exp(\gamma_{2n} z), \tag{18}$$

$$H_{\phi(3)} = \sum_{n=0}^{\infty} \frac{j\omega\epsilon_3}{\gamma_{3n}} Q_n G_n(\rho) \exp(-\gamma_{3n}(z - L)). \tag{19}$$

9.3 Matching of Tangential-Field Components

According to Maxwell's field equations, the tangential components of E_ρ and H_ϕ must be continuous across interfaces. If we match eqs. (9) and (10) at $z = 0$ we obtain the following equations

$$A_m + B_m = \delta_{m0} + \Gamma_m, \tag{20}$$

where $m = 0, 1, 2.....$. If we match eq. (10) and eq. (11) at $z = L$ we obtain

$$Q_m = \sum_{n=0}^{\infty} [A_n \exp(-\gamma_{2n} L) + B_n \exp(\gamma_{2n} L)] < G_m R_n >, \tag{21}$$

or

$$\vec{Q} = \mathbf{M_2}[\mathbf{M}_6 \vec{A} + \mathbf{M}_7 \vec{B}], \tag{22}$$

where

$$M_{(2)mn} =< G_m R_n >, \tag{23}$$

$$M_{(6)mn} = \exp(-\gamma_{2n} L), \tag{24}$$

$$M_{(7)mn} = \exp(\gamma_{2n} L). \tag{25}$$

If we match eqs. (17) and (18) at $z = 0$ we obtain

$$A_m - B_m = \frac{\epsilon_1 \gamma_{2m}}{\epsilon_2 \gamma_{1m}} [\delta_{m0} - \Gamma_m], \tag{26}$$

where $m = 0, 1, 2$. If we match eqs. (18) and (19) at $z = L$ we find

$$\frac{\gamma_{2n}}{\epsilon_2} \sum_{m=0}^{\infty} \frac{\epsilon_3}{\gamma_{3m}} Q_m < G_m R_n >= A_n \exp(-\gamma_{2n} L) - B_n \exp(\gamma_{2n} L), \tag{27}$$

or

$$\mathbf{M}_1 \vec{Q} = \mathbf{M}_6 \vec{A} - \mathbf{M}_7 \vec{B}, \tag{28}$$

where

$$M_{(2)mn} =< G_m R_n > \frac{\gamma_{2n}\epsilon_{r3}}{\gamma_{3m}\epsilon_{r2}}. \tag{29}$$

9.4 Solving for the Coefficients

We can solve for the coefficients in eqs (20) and (26) using

$$A_n = \frac{1}{2}\left[\delta_{n0}(1+\frac{\epsilon_{r1}\gamma_{2n}}{\epsilon_{r2}\gamma_{1n}}) + \Gamma_n(1-\frac{\epsilon_{r1}\gamma_{2n}}{\epsilon_{r2}\gamma_{1n}})\right], \tag{30}$$

and

$$B_n = \frac{1}{2}\left[\delta_{n0}(1-\frac{\epsilon_{r1}\gamma_{2n}}{\epsilon_{r2}\gamma_{1n}}) + \Gamma_n(1+\frac{\epsilon_{r1}\gamma_{2n}}{\epsilon_{r2}\gamma_{1n}})\right]. \tag{31}$$

Let

$$\vec{A} = \vec{C} + \mathbf{M_3}\vec{\Gamma}, \tag{32}$$

$$\vec{B} = \vec{D} + \mathbf{M_4}\vec{\Gamma}, \tag{33}$$

where

$$\mathbf{M}_{(3)mn} = \frac{1}{2}\left(1-\frac{\epsilon_{r1}\gamma_{2n}}{\epsilon_{r2}\gamma_{1n}}\right), \tag{34}$$

$$\mathbf{M}_{(4)mn} = \frac{1}{2}\left(1+\frac{\epsilon_{r1}\gamma_{2n}}{\epsilon_{r2}\gamma_{1n}}\right), \tag{35}$$

$$\vec{C} = \frac{1}{2}\left[\delta_{n0}(1+\frac{\epsilon_{r1}\gamma_{2n}}{\epsilon_{r2}\gamma_{1n}})\right], \tag{36}$$

$$\vec{D} = \frac{1}{2}\left[\delta_{n0}(1-\frac{\epsilon_{r1}\gamma_{2n}}{\epsilon_{r2}\gamma_{1n}})\right]. \tag{37}$$

We obtain the following equation for the permittivity given measured $\vec{\Gamma}$

$$[\mathbf{M_1M_2(M_6M_3+M_7M_4)-M_3+M_4)}]\Gamma = [\mathbf{I}-\mathbf{M_1M_2M_6}]\vec{C} - [\mathbf{I}+\mathbf{M_1M_2M_7}]\vec{D}, \tag{38}$$

or in terms of matrices and vectors

$$\mathbf{P}\cdot\vec{\Gamma} = \vec{T}. \tag{39}$$

Given measured results of the TEM mode Γ_0, we use Cramer's rule in eq. (39) to get an equation for ϵ_r^* of the form $\Gamma_0 = f(\epsilon_{3r})$.

For measurements, the reference plane must be transformed through the bead (b) and air (a) sections. The transformed reflection coefficient for the TEM mode is

$$\Gamma_{\text{trans}} = \Gamma_0 \exp\left(-2(\gamma_a L_1 + \gamma_b L_2)\right), \tag{40}$$

where L_1 and L_2 are the effective axial lengths of the air and bead sections of the connector. The bead is usually nonuniform, so an effective length needs to be determined from a standard measurement.

9.5 Integrals

$$G_n(\rho) = S_n J_1(k_{3n}\rho), \tag{41}$$

$$S_n = \frac{1}{\sqrt{\int_0^b \rho J_1^2(k_{3n}\rho)d\rho}} = \frac{\sqrt{2}}{bJ_1(k_{3n}b)}, \tag{42}$$

also

$$\int_0^b J_1(k_{3n}\rho)d\rho = \frac{1}{k_{3n}}, \tag{43}$$

$$< G_n R_0 >= \frac{1}{\sqrt{\ln(b/a)}} S_n \int_a^b J_1(k_{3n}\rho)d\rho = \frac{1}{\sqrt{\ln(b/a)}} S_n \frac{1}{k_{3n}} J_0(k_{3n}a), \tag{44}$$

and

$$< G_n R_m >= S_n \int_a^b \rho J_1(k_{3n}\rho) R_m(\rho)d\rho = S_n D_{mn}, \tag{45}$$

where the radial eigenfunctions are

$$\begin{aligned} R_n(\rho) = & \underbrace{C_0/\rho}_{\text{for } n=0 \text{ (TEM mode)}} \\ & = \underbrace{C_n[J_1(k_{2n}\rho)N_0(k_{2n}a) - N_1(k_{2n}\rho)J_0(k_{2n}a)]}_{n>0 (TM_{0n} \text{modes})}, \end{aligned} \tag{46}$$

where N_i, $i = 0, 1$, are the Bessel functions of the second kind and the constants C_n are obtained by requiring orthogonality [27], [28]:

$$\int_a^b \zeta R_m(b\zeta) R_n(a\zeta)d\zeta = \delta_{mn} \quad \text{m, n} = 0,\ 1,\ 2\ \ldots\ , \tag{47}$$

$$C_0 = \frac{1}{\sqrt{\ln(b/a)}}, \tag{48}$$

and

$$C_n = \sqrt{\frac{1}{\int_a^b \rho R_n^2(\rho)d\rho}} = \frac{\pi k_{2n}}{\sqrt{2}} \frac{1}{\sqrt{\frac{J_0^2(k_{2n}a)}{J_0^2(k_{2n}b)} - 1}}. \tag{49}$$

The coefficients $D_{mn}(\zeta) = \int_0^b \rho J_1(k_{3m}\rho) R_n(\rho)d\rho$ can be found analytically. For $n = 0$

$$D_{m0}(\zeta) = \frac{1}{\sqrt{\ln b/a}} \int_a^b J_1(k_{3m}\rho)d\rho = \frac{J_0(k_{3m}a)}{\sqrt{\ln b/a}} \frac{1}{k_{3m}}, \tag{50}$$

and otherwise

$$D_{mn}(k_{3n}) = \int_a^b \rho R_n(\rho) J_1(k_{3m}\rho) d\rho$$
$$= \frac{2}{\pi} \frac{C_n}{k_{2n}} \frac{k_{3m}}{k_{3m}^2 - k_{2n}^2} J_0(k_{3m}a). \tag{51}$$

10. Appendix D: Mixture Theories for Conductive Materials

Consider the effective conductivity σ_m from a material consisting of high σ_h and low conductivity σ_l. The volume fraction of the less conductive phase (σ_l) is θ for the various models we will review [29] (see figure 27).

The Maxwell-Wagner model can be envisioned as the effective conductivity for a space filled with coated spheres. The Maxwell-Wagner model for a high-conductivity coating on low-conductivity spheres is

$$\frac{\sigma_m - \sigma_h}{\sigma_m + 2\sigma_h} = \theta \frac{\sigma_l - \sigma_h}{\sigma_h + 2\sigma_l}. \tag{52}$$

The Maxwell-Wagner model for a low-conductivity coating on highly conducting spheres is

$$\frac{\sigma_m - \sigma_l}{\sigma_m + 2\sigma_l} = (1-\theta) \frac{\sigma_h - \sigma_l}{\sigma_l + 2\sigma_h}. \tag{53}$$

Bruggeman's equation for asymmetric media for high-conductive coating on low conductive spheres is

$$\frac{(\sigma_m - \sigma_l)^3}{\sigma_m} = (1-\theta)^3 \frac{(\sigma_h - \sigma_l)^3}{\sigma_h}, \tag{54}$$

and Bruggeman's equation for asymmetric media for low-conductive coating on highly conductive spheres is

$$\frac{(\sigma_m - \sigma_h)^3}{\sigma_m} = \theta^3 \frac{(\sigma_l - \sigma_h)^3}{\sigma_l}. \tag{55}$$

Bruggeman's equation for symmetric media filled with high and low conducting ellipsoids is

$$\theta \frac{(\sigma_l - \sigma_m)}{(\sigma_l + A\sigma_m)} + (1-\theta) \frac{(\sigma_h - \sigma_m)}{(\sigma_h + A\sigma_m)} = 0, \tag{56}$$

where A depends on the demagnetization coefficients of the ellipsoids and is 2 for spheres. None of the above described mixture equations model percolation behavior.

Particles in fluids are often modeled by Archie's law. If the particles occupy a volume fraction θ, then the effective conductivity is

$$\frac{\sigma_{eff} - \sigma_{part}}{\sigma_{solv} - \sigma_{part}} \left(\frac{\sigma_{solv}}{\sigma_{eff}} \right)^{L_a} = 1 - \theta, \tag{57}$$

a) Maxwell-Garnet, Asymmetric Bruggeman

b) Symmetric Bruggeman

Figure 27. The models used in the various mixture theories, with black denoting low-conductivity regions, and white the high-conductivity regions: (a) Maxwell-Garnet and asymmetric Bruggeman models, and (b) symmetric Bruggeman model.

where L_a is the effective depolarization factor. In the special case where $\sigma_{part} = 0$, we have Archie's law,

$$\sigma_{eff} = \sigma_{solv}(1-\theta)^{1/(1-L_a)}. \tag{58}$$

In highly conductive materials, the frequency dependence in ac conductivity can sometimes be modeled as a power-law:

$$\sigma_m \propto (\frac{\omega}{\omega_c})^n, \tag{59}$$

$$\epsilon_m \propto (\frac{\omega}{\omega_c})^{-m}, \tag{60}$$

where $m + n = 1$.

*U.S. GPO 2002-0-773-018/40217